34th Annual International Conference of the IEEE EMBS
San Diego, California USA, 28 August - 1 September, 2012

PET-CT based automated lung nodule detection

Norbert Zsoter, Peter Bandi, Gergely Szabo, Zoltan Toth, Ralph A. Bundschuh, Julia Dinges, Laszlo Papp

Abstract— **An automatic method is presented in order to detect lung nodules in PET-CT studies. Using the foreground and background mean ratio independently in every nodule, we can detect the region of the nodules properly. The size and intensity of the lesions do not affect the result of the algorithm, although size constraints are present in the final classification step. The CT image is also used to classify the found lesions built on lung segmentation. We also deal with those cases when nearby and similar nodules are merged into one by a split-up post-processing step. With our method the time of the localization can be decreased from more than one hour to maximum five minutes. The method had been implemented and validated on real clinical cases in Interview Fusion clinical evaluation software (Mediso). Results indicate that our approach is very effective in detecting lung nodules and can be a valuable aid for physicians working in the daily routine of oncology.**

I. INTRODUCTION

Positron Emission Tomography (PET) is one of the most important functional modalities in the field of nuclear medicine and oncology [1], [2], [3]. Combining PET with Computed Tomography (CT) brings great benefit to accurately localize lesions in the PET due to the anatomical information provided by CT. Lung cancer is especially the subject of oncological examinations, since it is one of the most common and dangerous cancer diseases in the world [3], [4]. Hence the early detection of lung nodules based on PET-CT is a key step to increase the survival ratio of individuals.

Most prior methods are based on global Standard Uptake Value (SUV) threshold which is either fixed or given by the user [2], [5], [6]. Obviously, these solutions do not guarantee that all lesions get the optimal local threshold value.

Other methods require a manually given initial threshold, which is further modified independently for all individual lesions based on their local lesion - background mean ratio [7]. Unfortunately these methods often operate with a fixed ratio given by the user which does not guarantee that all individual lesions are optimally segmented. Furthermore these methods still suffer from the issue of merging nearly located but independent lesions into one large region.

Our goal was to design an automated method which accurately detects and segments lung nodules based on multiple information derived from PET-CT. Our idea was to detect all local maxima positions inside of the PET and to perform region growing from them to find that region-specific threshold where the given region has the highest gradient. We considered several constraints such as maximum allowable size of a nodule. Furthermore we especially focused on detecting nearby, yet independent nodules as separate ones without merging them. Although our method operated with a low threshold, it was necessary only to filter out too small background noises. Nevertheless, this threshold value did not affect the final shape of our regions. We consequently derived tissue information from CT by adopting multiple fuzzy based tissue/organ segmentation approach to automatically detect the lungs inside of the CT. Using this information could help us to automatically classify detected lesions inside of the PET.

N. Zsoter, G. Szabo, P. Bandi and L. Papp are with Mediso Medical Imaging Systems Ltd., Baross str. 91-95, Budapest, Hungary, norbert.zsoter@mediso.hu

Z. Toth is with Scanomed Ltd., Budapest, Hungary

R. A. Bundschuh is with University of Wuerzburg, Wuerzburg, Germany

J. Dinges is with Technical University of Munich, Munich, Germany

II. MATERIALS AND METHODS

A. Image data

We collected 26 positive and 5 negative lung nodule PET-CT cases and their corresponding medical reports including findings localized by nuclear medicine specialists and result of pathological evaluation. The images represented the torso of the body which always fully included the lungs. PET images were attenuation and SUV corrected. The voxel resolution of our PET images was uniformly 4mm in all three directions. CT images had 0.98x0.98x3.17 voxel size, where the last value represented the spacing between axial slices. CT image values were Hounsfield corrected.

We denoted the PET and the CT images by $\mathcal{PT}$ and $\mathcal{CT}$ respectively.

B. PET Peak detection

Similarly to prior related work [8] we detected the local maxima positions (peaks) inside of the PET in order to determine the core of all potential hot spots.

The local maxima detection was performed by a three-dimensional mask having kernel size of $3 \times 3 \times 3$ voxels. A point was determined as peak position if it was the maximum of its neighbors determined by the above mask. Only those peaks were saved that had a greater value than a $T_{low} \in \mathbb{N}$ global minimum threshold value. T_{low} was initially set to the voxel value associated with 1 SUV. This value could be changed by the user and it was necessary for runtime minimization purposes. Based on relevant medical research, hot spots laid under this value were classified as local noises [5], [6]. The detected $\overline{p} \in \mathbb{N}^3$ peak point coordinates were stored in a $P \subset \left\{\mathbb{N}^3\right\}$ set.

978-1-4577-1787-1/12/$26.00 ©2012 IEEE

C. Initial PET region detection

The segmentation was an iterative process starting from the maximum count value of the PET ($\mathcal{PT}_{max}$) going until the above mentioned T_{low} value. The number of iterations was stored in $it \in \mathbb{N}$, where $it = 2000$ was chosen. The actual T_i threshold value in the i^{th} iteration was determined by eq. 1.

$$T_i = \mathcal{PT}_{max} - \left(i * \frac{\mathcal{PT}_{max} - T_{low}}{it} \right) \tag{1}$$

We performed a region growing in every i^{th} iteration from all $\overline{p} \in P$ peaks where $\mathcal{PT}(\overline{p}) \geq T_i$ was true. The region growing included only those positions into the given region that were greater or equal than the actual T_i. This way a simple isocount was determined for all peaks. The grown region coordinates from a given $\overline{p}$ peak point at a given T_i threshold value were denoted by $f_\rho(\overline{p}, T_i)$, where $f_\rho : \mathbb{N}^3, \mathbb{R} \rightarrow \left\{\mathbb{N}^3\right\}^*$.

During the region grow we recursively checked the 6 neighbors of the given peak. Every grown region was checked whether it reached a maximum volume which was stored in $MAX_v \in \mathbb{N}$. By default $MAX_v = 50000mm^3$ was chosen.

A morphological dilation was performed over a $f_\rho(\overline{p}, T_i)$ region by examining the 18 neighbors of its coordinates [9], [10] (excluding the 8 diagonal corners of the mask). Positions laid inside of the given dilated hull - not containing coordinates in $f_\rho(\overline{p}, T_i)$ - were denoted by $f_\delta(\overline{p}, T_i)$, where $f_\delta : \mathbb{N}^3, \mathbb{R} \rightarrow \left\{\mathbb{N}^3\right\}^*$.

We applied an $f_\mu : \left\{\mathbb{N}^3\right\}^* \rightarrow \mathbb{R}$ function which determined the mean values of $\mathcal{PT}$ laid on coordinates located in a $C \subset \left\{\mathbb{N}^3\right\}^*$ set as defined by eq. 2.

$$f_\mu(C) = \sum_{\overline{c} \in C} \frac{\mathcal{PT}(\overline{c})}{|C|} \tag{2}$$

We calculated the $\gamma_i^{\overline{p}}$ ratio of a $f_\rho(\overline{p}, T_i)$ region mean and its $f_\delta(\overline{p}, T_i)$ hull mean as defined by eq. 3.

$$\gamma_i^{\overline{p}} = \frac{f_\mu(f_\rho(\overline{p}, T_i))}{f_\mu(f_\delta(\overline{p}, T_i))} \tag{3}$$

We needed the $\gamma_i^{\overline{p}}$ ratio value because we wanted to log those ratio - threshold pairs where the given ratio was larger than any previously logged ratios. We assumed that logging these value pairs would aid us to choose that particular threshold for the given region which had the highest ratio value. We denoted the log set of a $\overline{p} \in P$ peak by $L^{\overline{p}} \subset \{(\mathbb{R}, \mathbb{R})\}^*$. If the actual $\gamma_i^{\overline{p}}$ was larger than any older logged $\gamma_j^{\overline{p}}$ where $j < i$ then the actual $(\gamma_i^{\overline{p}}, T_i)$ pair was stored in $L^{\overline{p}}$.

After the iterative process had finished, we had the log set of $(\gamma, \tau) \in L^{\overline{p}}$ pairs for all $\overline{p} \in P$ peak points. We determined the final $R^{\overline{p}} \subset \left\{\mathbb{N}^3\right\}^*$ region coordinates for all $\overline{p} \in P$ peak points by eq. 4.

$$R^{\overline{p}} = f_\rho \left(\overline{p}, \arg\max_\tau \left(\gamma | (\gamma, \tau) \in L^{\overline{p}} \right) \right) \tag{4}$$

TABLE I
ALGORITHMIC STEPS OF THE INITIAL PET REGION DETECTION STEP

1	$\forall 1 \leq i \leq it$:
2	*determine* T_i by eq. 1
3	$\forall \overline{p} \in P | \mathcal{PT}(\overline{p}) > T_i$:
4	*determine the region* of $\overline{p}$ by $f_\rho(\overline{p}, T_i)$
5	*determine* $f_\delta(\overline{p}, T_i)$
6	*determine* $\gamma_i^{\overline{p}}$ by eq. 2.
7	if $\gamma_i^{\overline{p}} > \arg\max_\gamma(\gamma | (\gamma, \tau) \in L^{\overline{P}})$
8	$L^{\overline{p}} = L^{\overline{p}} \cup (\gamma_i^{\overline{p}}, T_i)$

For detailed explanation of the PET lesion detection algorithm see Tab. I.

D. PET region post-processing

The result of the above algorithm required three post-corrections: handle regions that were equal, handle regions having intersection, and handle too small regions.

Equal regions typically appeared when some nearby regions converged to the same threshold value and hence they became equal. This situation appeared when the given lesion had a lot of local maxima positions that were independently located and handled by our method. Obviously, this case resulted redundant regions, hence all of them except one were classified as false regions.

The second case appeared when e.g. an $R^{\overline{l}}$ region ($\overline{l} \in P$) converged to a threshold value in such a way that it included other nearby regions as well. According to the specification of physicians, it was desired to separate these regions. We checked whether a smaller $R^{\overline{s}}$ region (where $\overline{s} \in P$) had a larger γ than the larger $R^{\overline{l}}$ region had. If this condition met, we iteratively increased the threshold value of $R^{\overline{l}}$ according to its logged τ threshold list until the regions became independent. We performed this check for all regions until there were regions having intersection.

For detailed explanation of the first two post-processing steps see Tab. II.

As the last step of the post-processing, all regions were classified as false ones if their volume was smaller than $MIN_v \in \mathbb{R}$ value. According to initial trials we chose $MIN_v = 100mm^3$ as a minimum volume, which was slightly larger than the area of one PET voxel. For results of current step see Fig. 1.

The final post-processed regions were denoted by $R^{\overline{q}} \subset \left\{\mathbb{N}^3\right\}^*$ for all $\overline{q} \in Q$ peaks. $Q \subseteq P$ was the set of those peaks whose region was classified as a true one.

E. CT based fuzzy affinity map generation

Our strategy was to generate four fuzzy affinity maps for lungs, fat, muscle and bone respectively [11], [12]. These maps were necessary to decide whether a detected PET nodule laid inside of the lungs or not. Due to the presence of the heart, fat and muscle Hounsfield valued regions were present between the lungs. These regions were quite similar to the respiratory tracts and the bronchial tree as well. Due to these reasons, simple Hounsfield unit based threshold techniques

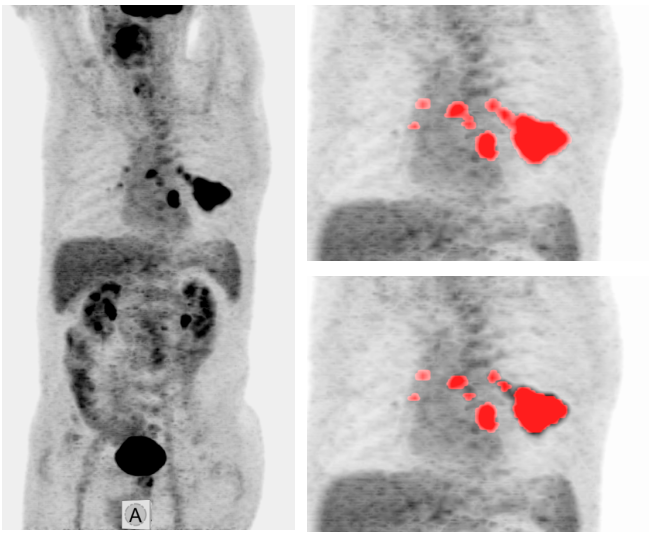

Fig. 1. Left: Maximum Intensity Projection (MIP) view of the original PET volume. Top right: Merged regions before the post-processing step. Bottom right: Result of the region intersection correction.

TABLE II
ALGORITHMIC STEPS OF THE PET REGION POST-PROCESSING STEP

1	$\forall \overline{p} \in P$:
2	$\forall \overline{q} \in P \vert \overline{q} \neq \overline{p}$:
3	if $R^{\overline{q}} = R^{\overline{p}}$:
4	*classify* $R^{\overline{q}}$ *as false region*
5	else if $R^{\overline{q}} \subset R^{\overline{p}}$:
6	if $\left(\max_{\gamma}((\gamma,\tau) \in L^{\overline{q}}) > \max_{\gamma}((\gamma,\tau) \in L^{\overline{p}}) \right)$:
7	$\hat{R}^{\overline{p}} = R^{\overline{p}}$
8	while $\hat{R}^{\overline{p}} \cap R^{\overline{q}} \neq \oslash$:
9	$L^{\overline{p}} = L^{\overline{p}} \setminus \arg\max_{(\gamma,\tau)}(\gamma \vert (\gamma,\tau) \in L^{\overline{p}})$
10	$\hat{R}^{\overline{p}} = f_{\rho}(\overline{p}, \arg\max_{\tau}(\gamma \vert (\gamma,\tau) \in L^{\overline{p}})$
11	$R^{\overline{p}} = \hat{R}^{\overline{p}}$

would not have been relevant. Furthermore, threshold would classify lung regions as air regions outside of the body and vice versa. Additionally, ribs covered the lungs from the outer direction of the body, hence bones had to be separated as well.

We wanted to compare the four fuzzy affinity maps to one another instead of operating with one lung affinity map and its corresponding threshold value. Based on initial trials, the latter solution would not have been accurate, since a threshold value of an affinity map would have changed in every patient images. Nevertheless, comparing four fuzzy affinity maps at common positions could lead us to a safer decision since their relative values could clearly describe the given tissue/organ type.

1) Adaptive fuzzy segmentation framework: We used the adaptive fuzzy approach proposed in [11], [12]. This technique required seed points to generate a fuzzy affinity map having real values between 0.0 and 1.0.

2) Lung affinity map generation: Since the CT images were Hounsfield corrected, a simple threshold at -200 HU was enough to separate the air and the body. On the binary threshed body-air mask the lungs were classified as air regions and they always had a a connection with the outside air region due to the esophagus. To close the esophagus, a three dimensional morphological dilation was performed with a $3 \times 3 \times 3$ kernel four times. According to initial trials, this amount of dilation always closed the esophagus but also decreased the region of the lungs. This effect was negligible for us, since we were seeking for seed points of the lungs, not their exact shape. Based on the dilated mask the two largest regions inside of the body were chosen and their center of gravity was detected as lung seed points. Additionally, a bounding box over the eroded lungs was determined but its size was corrected in all 6 directions by 4 voxels to balance the shrinking effect caused by the four dilation steps.

Based on the seed point pairs the above fuzzy segmentation algorithm was performed and the result affinity map was stored in $\mathcal{CT}^{L}$ image.

3) Fat, muscle and bone affinity map generation: To generate the fat fuzzy affinity map, we selected a seed point inside of the body and outside of the bounding box of the lung. The seed point for the fat was selected from the Hounsfield unit interval of $-100, -90$. Muscle seed points were consequently selected from the value range of $40, 60$ and bone seed points were chosen from the middle axial slice where values were larger than 150. The final fat, muscle and bone affinity maps were denoted by $\mathcal{CT}^{F}$, $\mathcal{CT}^{M}$ and $\mathcal{CT}^{B}$ respectively.

F. PET lung nodule classification

We determined the dilated hull of all $R^{\overline{q}}$ valid lesions as described in section II-D and denoted as $H^{\overline{q}} = f_{\delta}(\overline{q}, \tau)$ where $\tau = \max_{\tau}((\gamma,\tau) \in L^{\overline{q}})$. We determined the mean of the fuzzy affinity values laid under the coordinates of the given $H^{\overline{q}}$ hull for all four fuzzy affinity maps respectively. These mean values were consequently denoted as $\mu_{L}^{\overline{q}}$, $\mu_{F}^{\overline{q}}$, $\mu_{M}^{\overline{q}}$ and $\mu_{B}^{\overline{q}}$ for lung, fat, muscle and bone affinity maps.

The reason of choosing hull coordinates was that lung nodules normally had non-lung Hounsfield values. Nevertheless, their surrounding CT values laid inside of the lungs. Hence collecting the mean fuzzy value from the affinity maps only in the hull coordinates led us to a more accurate classification.

An $R^{\overline{q}}$ region was classified as lung nodule if its $\mu_{L}^{\overline{q}}$ was maximal among the four mean values. For results of current step see Fig. 2 and Fig. 3.

G. Validation

The validation was performed in Interview Fusion clinical evaluation software developed by Mediso where the above method was implemented. Two nuclear medicine specialists compared the results of our method to prior medical reports of our data sets. Our method sorted the classified lung nodules based on their γ ratio. The specialists could change the position of a slider which provided a threshold for the

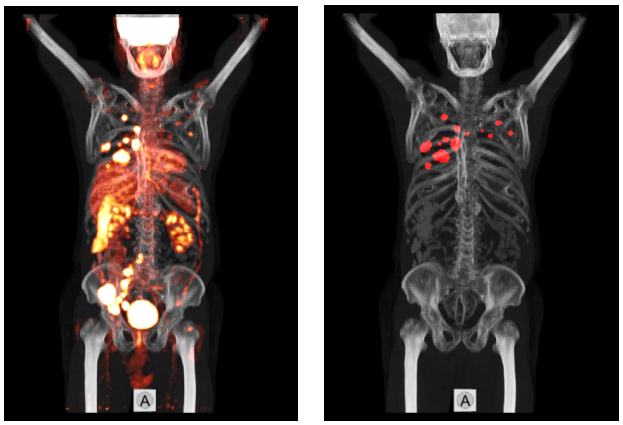

Fig. 2. Left: Original PET and CT fused in a MIP view. Right: The segmented lung nodules with the CT in a MIP view.

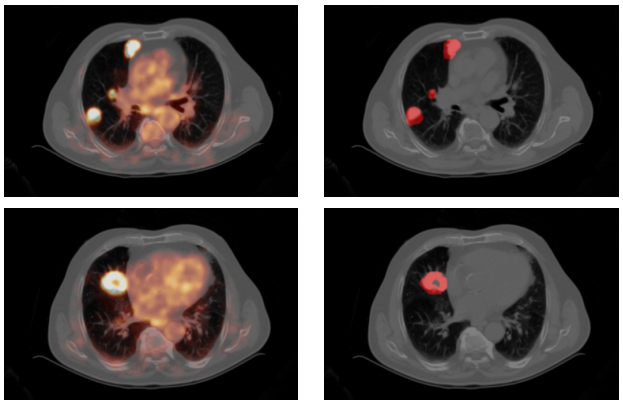

Fig. 3. Left column: Axial slices of a positive case representing lung nodules on fused PET-CT views. Right column: Corresponding segmented lung nodules fused with the CT. Note the necrobiotic nodule on the bottom images, hence a hole is present in the middle of its mask.

γ values. According to initial trials we set the value of this slider to 1.6. Those lesions having less values than the actual ratio threshold were classified as false regions. We logged the number of γ threshold slider modifications. Further parameters of the algorithm could be changed by the specialists as well such as the T_{low}, τ, MIN_v and MAX_v.

III. RESULTS

Our method successfully detected 96% of all previously reported lesions inside of lungs without user interactions. All of these nodules were previously reported. Additionally it also detected 5 false negative lesions in overall 3 studies. No nodules were detected in the 5 negative cases. A fully automated runtime took average 1 minute per study.

By modifying some parameters we could successfully detect all 51 lesions in the 26 positive cases. In this case we could decrease the number of false positive lesions to 1. Modifying T_{low}, was necessary 2 times, since some very low SUV valued benign lesions [1] were missing, although there was no consensus by the physicians whether these lesions had to be detected or not. Modification of τ was 5 times necessary, where the size of the region was not exactly the desired one (although the region itself was detected). Modifying the ratio threshold slider was 2 times necessary. These modifications normally took 3-7 seconds, since our method modified the list of true regions in real-time. No manual MIN_v, MAX_v modification was necessary.

IV. CONCLUSIONS AND FUTURE WORKS

A. Conclusions

We have presented a fast and accurate method to automatically detect lung nodules on PET-CT images. According to the ratio of misclassification manual interventions of our method, it can be considered to be automated, although in some cases manual parameter modifications were necessary. The background ratio based ordering of the lesions seems to be a logical aid for users. It took average 5-6 minutes (including manual interventions) to localize nodules in a patient with our method which is comparable to the necessary time (60-90 minutes) to perform the manual evaluation.

B. Future Works

Our algorithm will be extended to deal with lymph nodes and melanoma as well. The four fuzzy affinity maps could be used for localizing lesions inside of other tissues as well. Knowing the type of cancer to detect, parameters of the algorithm could be fine-tuned to the specific needs.

REFERENCES

[1] F. G. Duhaylongsod, V. J. Lowe, E. F. Patz, et al., Detection of primary and recurrent lung cancer by means of F-18 fluorodeoxyglucose positron emission tomography (FDG PET), *J Thorac Cardiovasc Surg*, vol. 110, 1995, pp. 130-140.

[2] M. Khalaf, H. Abdel-Nadi, J. Baker, et al., Relation between nodule size and 18F-FDG-PET SUV for malignant and benign pulmonary nodules, *J Hemat Oncol*, 2008, pp. 1-13.

[3] A. Grgic, Y. Yueksel, A. Groeschel, et al., Risk stratification of solitary pulmonary nodules by means of PET using 18F-fluorodeoxyglucose and SUV quantification, *Eur J Nucl Med Mol Imaging*, vol. 37, 2010, pp. 1087-1094

[4] S. Srinivas, A. Cohen, Improving accuracy of PET/CT in the diagnosis of the solitary pulmonary nodule, *J Nucl Med*, vol. 49, 2008, pp. 246

[5] Y. Hashimoto, T. Tsujikawa, C. Kondo, et al.,Accuracy of PET for Diagnosis of Solid Pulmonary Lesions with 18F-FDG Uptake Below the Standardized Uptake Value of 2.5, *J Nucl Med*, vol. 47, 2006, 426-431

[6] D. Hellwing, T. P. Graeter, D. Ukena, et al., 18F-FDG PET for Mediastinal Staging of Lung Cancer: Which SUV Threshold Makes Sense?, *J Nucl Med*, vol. 48, 2007, pp. 1761-1766.

[7] F. Hofheinz, C. Poetzsch, L. Oehme, et al., Automatic volume delineation in oncological PET Evaluation of a dedicated software tool and comparison with manual delineation in clinical data sets, *Nuklearmedizin*, vol. 51, 2012, pp. 1-8.

[8] L. Papp, N. Zsoter, C. Loh, et al., Automated lymph node detection and classification on breast and prostate cancer SPECT-CT images, *IEEE Conf Proc IEEE Eng Med Biol Soc*, 2011, pp. 3431-3434.

[9] R. M. Haralick, S. R. Sternberg, X. Zhuang, Image Analysis Using Mathematical Morphology, *IEEE Tr Patt Anal Mach Int*, vol. 9, 1987, pp. 532-550.

[10] S. Hu, E. A. Hoffman, J. M. Heinhardt, Automatic lung segmentation for accurate quantitation of volumetric X-ray CT images,*IEEE Tr Med Img*, vol. 20, 2001, pp. 490 - 498.

[11] J. K. Udupa, S. Samarasekera, Fuzzy Connectedness and Object Definition: Theory, Algorithms, and Applications in Image Segmentation, *Graph Mod Img Proc*, vol. 58, no. 3, 1996, pp. 246-261.

[12] K. C. Ciesielski, J. K. Udupa, Affinity functions in fuzzy connectedness based image segmentation II: Defining and recognizing truly novel affinities, *Comp Vis Img Underst*, vol. 114, 2010, 155-166.